

Crystal phase and architecture engineering of lotus thalamus-shaped Pt-Ni anisotropic superstructures for highly efficient electrochemical hydrogen evolution

Zhang, Zhicheng; Liu, Guigao; Cui, Xiaoya; Chen, Bo; Zhu, Yihan; Gong, Yue; Saleem, Faisal; Xi, Shibo; Du, Yonghua; Borgna, Armando; Lai, Zhuangchai; Zhang, Qinghua; Li, Bing; Zong, Yun; Han, Yu; Gu, Lin; Zhang, Hua

2018

Zhang, Z., Liu, G., Cui, X., Chen, B., Zhu, Y., Gong, Y., ...Zhang, H. (2018). Crystal phase and architecture engineering of lotus-thalamus-shaped Pt-Ni anisotropic superstructures for highly efficient electrochemical hydrogen evolution. *Advanced Materials*, 30(30), 1801741-. doi:10.1002/adma.201801741

<https://hdl.handle.net/10356/88887>

<https://doi.org/10.1002/adma.201801741>

This is the peer reviewed version of the following article: Zhang, Z., Liu, G., Cui, X., Chen, B., Zhu, Y., Gong, Y., ...Zhang, H. (2018). Crystal phase and architecture engineering of lotus-thalamus-shaped Pt-Ni anisotropic superstructures for highly efficient electrochemical hydrogen evolution. *Advanced Materials*, 30(30), 1801741-. doi:10.1002/adma.201801741, which has been published in final form at <https://dx.doi.org/10.1002/adma.201801741>. This article may be used for non-commercial purposes in accordance with Wiley Terms and Conditions for Use of Self-Archived Versions.

DOI: 10.1002/ ((please add manuscript number))

Article type: Communication

Crystal Phase and Architecture Engineering of Lotus Thalamus-Shaped Pt-Ni Anisotropic Superstructures for Highly Efficient Electrochemical Hydrogen Evolution

By Zhicheng Zhang,¹ Guigao Liu,¹ Xiaoya Cui,¹ Bo Chen,¹ Yihan Zhu,² Yue Gong,³ Faisal Saleem,¹ Shibo Xi,⁴ Yonghua Du,⁴ Armando Borgna,⁴ Zhuangchai Lai,¹ Qinghua Zhang,³ Bing Li,⁵ Yun Zong,⁵ Yu Han,⁶ Lin Gu,³ and Hua Zhang^{1,}*

Zhicheng Zhang, Guigao Liu, Xiaoya Cui, Bo Chen, Yihan Zhu, Yue Gong, Faisal Saleem, Shibo Xi, Yonghua Du, Armando Borgna, Zhuangchai Lai, Qinghua Zhang, Bing Li, Yun Zong, Yu Han, Lin Gu, and Hua Zhang

Dr. Z. Zhang, Dr. G. Liu, X. Cui, Dr. B. Chen, Dr. F. Saleem, Z. Lai, Prof. H. Zhang

¹Center for Programmable Materials, School of Materials Science and Engineering, Nanyang Technological University, 50 Nanyang Avenue, Singapore 639798, Singapore.

*Email: hzhang@ntu.edu.sg. Website: <http://www.ntu.edu.sg/home/hzhang/>

Prof. Y. Zhu,

²Department of Chemical Engineering, Zhejiang University of Technology, Hangzhou 310014 (China)

Y. Gong, Prof. L. Gu

³Beijing National Laboratory for Condensed Matter Physics, Institute of Physics, Chinese Academy of Sciences. Collaborative Innovation Center of Quantum Matter. School of Physical Sciences, University of Chinese Academy of Sciences, Beijing 100190 (China)

Dr. S. Xi, Dr. Y. Du, Prof. A. Borgna

⁴Institute of Chemical and Engineering Sciences, A*STAR (Agency for Science, Technology and Research), Singapore 627833 (Singapore)

Dr. B. Li, Dr. Y. Zong

⁵Institute of Materials Research and Engineering (IMRE), A*STAR (Agency for Science, Technology and Research), 2 Fusionopolis Way, Innovis #08-03, Singapore 138634, Singapore.

Prof. Y. Han

⁶Advanced Membranes and Porous Materials Center, Physical Sciences and Engineering Division, King Abdullah University of Science and Technology, Thuwal 23955-6900 (Saudi Arabia)

Keywords: Pt-Ni alloy, anisotropic structure, crystal structure, electrocatalysis, hydrogen evolution reaction.

The rational design and synthesis of anisotropic three-dimensional nanostructures with specific composition, morphology, surface structure and crystal phase is of significant importance for their diverse applications. Here, we report the synthesis of well-crystalline lotus thalamus-

shaped Pt-Ni anisotropic superstructures (ASs) via a facile one-pot solvothermal method. The Pt-Ni ASs with Pt-rich surface are composed of one Ni-rich “core” with face-centered cubic (*fcc*) phase, Ni-rich “arms” with hexagonal close-packed (*hcp*) phase protruding from the core, and facet-selectively grown Pt-rich “lotus seeds” with *fcc* phase on the end surfaces of the “arms”. Impressively, this unique Pt-Ni ASs exhibit superior electrocatalytic activity and stability towards the hydrogen evolution reaction under alkaline conditions compared to the commercial Pt/C and previously reported electrocatalysts. The obtained overpotential is as low as 27.7 mV at current density of 10 mA cm⁻², and the turnover frequency (TOF) reaches 18.63 H₂ s⁻¹ at the overpotential of 50 mV. Our work provides a new strategy for the synthesis of highly anisotropic superstructures with a spatial heterogeneity to boost their promising application in catalytic reactions.

The rational design and synthesis of anisotropic three-dimensional (3D) architectures with complicated structures and promising functionalities have drawn considerable attention in recent years.^[1-3] Delicate control of the spatial composition, morphology, surface structure and crystal phase in such 3D nanomaterials is of great importance for their diverse applications.^[1] To date, various strategies, including seed-mediated growth,^[2] oxidative etching,^[3] self-assembly of building blocks^[4] and site-selective growth,^[5] have been developed to synthesize anisotropic 3D nanostructures. However, it still remains a great challenge to prepare anisotropic 3D nanostructures with desired chemical composition, surface structure, and crystal phase for specific applications, which are significant not only in fundamental studies, but also in practical applications.

Recently, anisotropic Pt-based nanostructures have attracted increasing research interests in the electrocatalysis because of their inherent physical and chemical properties originating from their unique structures.^[2,3] In order to enhance the electrocatalytic activity of Pt-based anisotropic nanomaterials, various approaches, including alloying Pt with earth-abundant

transition metals,^[3] engineering crystal phase of Pt-based alloys,^[6] shaping Pt-based nanostructures^[3,7,8] and constructing Pt-based hybrid nanomaterials,^[9-11] have been developed. Particularly, the anisotropic 3D Pt-based nanostructures with Pt-rich surface or unusual crystal phase are effective to improve their electrocatalytic activity. For example, Pt-Ni nanoframes with Pt-rich surface^[3] and Pt-Ni nanomultipods with novel hexagonal close-packed (*hcp*) phase^[6] have been reported to exhibit enhanced electrocatalytic activities towards hydrogen evolution reaction (HER) under alkaline conditions. Therefore, it is critically important to rationally design and synthesize novel anisotropic 3D structures possessing both Pt-rich surface and unusual crystal phase in order to further enhance their HER performance.

Herein, for the first time, we report a facile one-pot solvothermal method to synthesize well-crystalline lotus thalamus-shaped Pt-Ni anisotropic superstructures (ASs), referred to as Pt-Ni ASs. The obtained Pt-Ni AS with the spatial heterogeneity of compositional elements and crystal structures is composed of one Ni-rich “core” with face-centered cubic (*fcc*) phase, several Ni-rich “arms” with *hcp* phase protruding from the core, and facet-selectively grown Pt-rich “lotus seeds” with *fcc* phase on the end surfaces of the “arms” (Figure 1 and Figure S1). It is worth mentioning that the entire surface of Pt-Ni AS is Pt-rich. Impressively, the obtained Pt-Ni ASs exhibit superior electrocatalytic activity and stability towards HER under alkaline conditions compared to the commercial Pt/C and previously reported electrocatalysts.

The detailed experiment for the synthesis of the Pt-Ni ASs is described in Supporting Information. The representative high-angle annular dark-field scanning transmission electron microscopy (HAADF-STEM) (Figure 1a, b and Figure S1a) and scanning electron microscopy (SEM) images (Figure S1b) show that the obtained products consist of branched structures. Each branch resembles the thalamus of lotus (Figure S1c), i.e., some sharp-shaped nanoparticles selectively grown on the end surface of the “arm” (Figure S1d). TEM images show that the length of the “arm” is about 40 nm (Figure 1a, inset). The height of deposited nanoparticles, i.e., “lotus seeds”, is sub-10 nm (Figure 1a, inset). Therefore, the obtained Pt-Ni ASs display

the highly anisotropic feature. Figure 1c shows the aberration-corrected HAADF-STEM image of the typical “lotus seed” and the “arm” of Pt-Ni ASs. The “arm” shows the atom stacking mode of *hcp* structure, i.e., “ABAB”, along the $[001]_h$ close-packed direction (Figure 1c–e),^[12–14] whereas the “lotus seed” exhibits a characteristic stacking sequence of “ABCABC” along the $[111]_f$ close-packed direction (Figure 1c, f and g), adopting the conventional *fcc* structure.^[4,12,15] Moreover, twin boundaries along the $[001]_h/[111]_f$ directions are observed in the transition region between the “arm” and the “lotus seed” (Figure 1c). Figure 1h shows the aberration-corrected HAADF-STEM image of the “arm” along the $[100]_h$ zone axis. Owing to the different atomic number between Pt ($Z = 78$) and Ni ($Z = 28$), it is easy to distinguish Pt and Ni atoms by the Z-contrast in the HAADF-STEM images (Figure 1h), i.e., the brighter atoms are Pt and the darker ones are Ni. The enrichment of brighter atoms on the surface indicates Pt-rich surface in the “arm”. The fast Fourier transform (FFT) patterns (Figure 1i and k) and magnified aberration-corrected HAADF-STEM images (Figure 1j and l) of the “arm” confirm its *hcp* phase. The continuous lattice alignment from the backbone to the shell in the “arm” indicates their epitaxial growth (Figure 1h, j and l). Importantly, some low-coordinate atomic steps can be identified on the side surface of the “arm” (Figure 1h). The “core” of the Pt-Ni AS possesses a polyhedral morphology (Figure 1m and n), serving as a central node to grow the “arms” (Figure S1d). The X-ray diffraction (XRD) patterns further confirm the co-existence of *fcc* and *hcp* phases, which are 37.2 wt% and 62.8 wt%, respectively, in the Pt-Ni ASs (Figure S2 and Table S1). The chemical composition of the Pt-Ni ASs was measured by the inductively coupled plasma optical emission spectrometry (ICP-OES) and the energy-dispersive X-ray spectroscopy (EDS), which gave very similar Pt/Ni atomic ratios, i.e., 18.4/81.6 and 18.6/81.4 (Figure S3), respectively. The HAADF-STEM and the corresponding EDS elemental mapping images reveal the Pt-rich surface of the Pt-Ni ASs (Figure 1o).

A HAADF-STEM tilt series for an individual Pt-Ni AS was collected, aligned and reconstructed to visualize its three-dimensional (3D) architecture (Figure S4 and Movie S1).

From the reconstructed 3D visualization of the nanostructure by isosurface rendering (Figure S4a–f), the Pt-Ni AS is composed of four “arms” protruding from the “core” with some “lotus seeds” selectively grown on their end surfaces. The “lotus seeds” are Pt-rich, as evidenced by the slice of the tomogram and their segmented volume (Figure S4i). Moreover, a Pt-rich core can be identified at the central region of thin slices sectioned from the tomogram (Figure S4g and h). These results are consistent with the aforementioned ones (Figure 1 and Figure S1).

The X-ray absorption near-edge structure (XANES) and the extended X-ray absorption fine structure (EXAFS) were performed to investigate the local atomic and electronic structures of the Pt-Ni ASs. Figure 2a shows the Pt L_3 -edge XANES spectra of the Pt-Ni ASs, Pt foil and PtO_2 . Note that Pt foil and PtO_2 are used for reference. The intensity of the white line peak at about 11.56 keV for the Pt-Ni ASs is similar to that of the Pt foil, indicating the metallic state of Pt in the Pt-Ni ASs, which is consistent with the Pt 4f X-ray photoelectron spectroscopy (XPS) spectra of the Pt-Ni ASs (Figure 2e). The main peak in the Pt L_3 -edge FT-EXAFS spectra represents the nearest coordination shells of Pt atoms, which was well reproduced through a fitting using Pt-Ni and Pt-Pt paths (Figures S5 and S6 and Table S2). The shorter atom distance of the main peak in the Pt-Ni ASs suggests the shorter bond length than that of the Pt foil (Figure 2b), owing to the heteroatomic interaction in binary alloy nanostructures.^[16–18] The discrepancy of the oscillations in k space also suggests the different coordination environment of Pt in the Pt-Ni ASs and the Pt foil (Figure S7). The Ni K-edge XANES spectra of the Pt-Ni ASs, NiO, and the Ni foil are shown in Figure 2c, in which NiO and Ni foil are used for reference. It is worth mentioning that the Ni foil crystallizes in an *fcc* structure, whereas the Ni in Pt-Ni ASs mainly possesses an *hcp* structure, which has a larger nearest Ni-Ni distance (around 2.63 Å) compared to Ni foil (around 2.44 Å) (Figure 2d). The fitting result shows that the Ni in the Pt-Ni ASs is predominant in the metallic state (Figure S8 and Table S3). However, in the Ni 2p XPS spectra of the Pt-Ni ASs (Figure 2f), the peak corresponding to Ni^{2+} is even higher than that corresponding to metallic Ni, indicating the surface oxidation of Ni. The peak located

between 1.6 and 2.9 Å in the Ni K-edge FT-EXAFS spectra of the Pt-Ni ASs can be well reproduced through the fitting using Ni-Ni and Ni-Pt scattering paths (Figure S9 and Table S3).

In order to study the formation mechanism of Pt-Ni ASs, the time-dependent experiments were conducted. At the reaction time of 2 h, the faceted polyhedron-shaped nanoparticles with size of about 10 nm were obtained (Figure 3a and Figure S10). The EDS result shows that the Pt/Ni atomic ratio is about 3.2/96.8 (Figure 3f and Figure S11). As the reaction continuously proceeded, the branched nanostructures consisting of “arms” with length of about 20 nm were formed at the reaction time of 4 h (Figure 3b). The EDS result (Figure 3f and Figure S12), the HAADF-STEM and the corresponding EDS elemental mapping images (Figure S13) show that the product is Ni-rich, giving the Pt/Ni atomic ratio of 2.1/97.9. The XRD pattern shows that the product possesses an *hcp* phase (Figure 3g). At the reaction time of 6 h, the branched nanostructures further grew with longer “arms” of about 40 nm (Figure 3c and Figure S14). As shown in Figure S14, the “core” shows an *fcc* phase, whereas the “arm” possesses an *hcp* phase. Significantly, in the transition region between the “core” and the “arm”, there are twin boundaries. The EDS result shows that the Pt/Ni atomic ratio is about 4.3/95.7 (Figure 3f and Figure S15). The HAADF-STEM and the corresponding EDS elemental mapping images reveal the uniform distribution of Pt on the surface of the product (Figures S16 and S17). The XRD pattern shows that the product retains the *hcp* phase (Figure 3g). When the reaction time reached 9 h, some sharp-shaped nanoparticles selectively grew on the end surfaces of the “arms” (Figure 3d). The Pt/Ni atomic ratio was increased to 10.5/89.5, as shown by the EDS pattern (Figure 3f and Figure S18). The HAADF-STEM and the corresponding EDS elemental mapping images demonstrate the formation of Pt-rich surface of the product (Figure S19). The XRD pattern shows the appearance of *fcc* phase, co-existing with *hcp* phase (Figure 3g and h). Finally, at the reaction time of 14 h, the well-crystalline lotus thalamus-shaped Pt-Ni anisotropic superstructures with Pt/Ni atomic ratio of about 18.6/81.4 (Figure 3f and Figure S3), i.e., Pt-Ni ASs, were obtained (Figure 1 and Figure S1). The XRD pattern of Pt-Ni ASs is similar to that

of the product obtained at the reaction time of 9 h (Figure 3g and h), indicating their mixed *hcp/fcc* crystal phases.

Based on the aforementioned time-dependent structure evolution, we proposed a possible mechanism for the synthesis of Pt-Ni ASs. As schematically illustrated in Figure 3e, the Ni-rich polyhedral nanostructures were first formed (Figure 3a and e-1). As reported, the formaldehyde can be decomposed into CO and H₂ at elevated temperature.^[4,19-21] The produced H₂ and oleylamine in the reaction solution could facilitate the preferential reduction of Ni²⁺ ions,^[4,19] although the standard redox potential of Ni²⁺/Ni (-0.25 V) is more negative than that of Pt²⁺/Pt (1.18 V).^[4,22,23] Then, the polyhedral Ni-rich nanostructures grew into branched structures (Figure 3b and e-2), probably originating from the polymorphism of Ni.^[24] With the increase of reaction time, the branched nanostructures became larger (Figure 3c and e-3). During the aforementioned evolution process, a galvanic replacement reaction between Ni-rich branched nanostructures and Pt precursor (Pt(acac)₂) took place on the whole surfaces of Ni-rich branched nanostructures. Simultaneously, the Ni²⁺ ions (from the dissolution of Ni-rich branched nanostructures) and Pt²⁺ ions (from Pt(acac)₂) were reduced by the reductants in the solution. Subsequently, the resulting Ni and Pt atoms selectively deposited on the end surfaces, i.e., {001} planes, of the “arm” rather than its side surfaces, i.e., {011} planes (Figure 3d and e-4 and Figure S1d). As known, the surface energy, γ , of *hcp* metal nanostructures follows the order of {001} < {100} < {110} < {111}.^[20,25] Therefore, the selective deposition of Pt and Ni atoms should occur on the {011} planes rather than on the {001} planes of the “arms”. However, in our experiment, the preferential deposition was not observed on the {011} planes of the “arms” but on the {001} planes instead. This might be due to the strong capping effect of benzoin or oleylamine, acting as the facet-selective adsorption reagent on the side surface of the “arms”.^[6,24] As the reaction proceeded, the final product, i.e., Pt-Ni ASs, was obtained at reaction time of 14 h (Figure 1). It is worth mentioning that the Ni-rich polyhedral nanostructures were first formed during the shape evolution process (Figure 3a and e-1),

whereas the “core” in the Pt-Ni ASs is Pt-rich (Figure S4g and h). This could be attributed to the subsequent galvanic replacement reaction between metallic Ni and Pt^{2+} ions in the solution.

The chlor-alkali industry and water-alkali electrolysis are the main sources for electrocatalytic hydrogen production.^[9-11] However, the HER activities of Pt catalysts in alkaline solution are usually about two to three orders of magnitude lower than those in acidic solution.^[9,11] Therefore, it is very urgent to develop advanced electrocatalysts with superior HER activity in alkaline solution. As a proof-of-concept application, we evaluated the electrocatalytic HER performance of Pt-Ni ASs in 1.0 M KOH aqueous solution and compared it with the commercial Pt/C catalyst (20 wt% Pt on Vulcan XC-72R carbon, Figure S20). The linear sweep voltammetry (LSV) curves (with Ohmic drop correction) of Pt-Ni ASs with the optimum Pt loading of about 0.017 mg cm^{-2} at scan rate of 5 mV s^{-1} (Figure S21) is shown in Figure 4a. Pt-Ni ASs show a nearly equal onset potential to Pt/C, but present a much higher current increase rate, indicating the superior HER activity. Accordingly, a rather small Tafel slope of 27 mV dec^{-1} was observed for Pt-Ni ASs, which is 17 mV dec^{-1} lower than that of Pt/C (44 mV dec^{-1}) and even much lower than other previously reported HER catalysts (Figure 4b, Figure S22 and Table S4). The low Tafel slope of Pt-Ni ASs suggests that the recombination of chemisorbed hydrogen atoms on their surface is the rate-limiting step and the HER reaction involves the Volmer-Tafel mechanism.^[26] Furthermore, the exchange current density of Pt-Ni ASs, obtained from the Tafel plot, reaches as high as 1.35 mA cm^{-2} , which is higher than that of Pt/C (1.29 mA cm^{-2}) (Figure 4c), reflecting their superior intrinsic electrocatalytic activity. The mass activity (Figure 4d) and specific activity (Figure S23) were obtained by normalizing the current densities with respect to the mass loading of Pt (0.017 mg cm^{-2}) and the electrochemically active surface area (ECSA) (Figure S24), respectively. Remarkably, the Pt-Ni ASs show significantly higher mass and specific activities than does Pt/C (Figure 4d and Figure S23). Specifically, at the overpotential of 70 mV, the mass and specific activities of Pt-

Ni ASs were $2.80 \text{ A mg}_{\text{Pt}}^{-1}$ and 13.7 mA cm^{-2} , which are about 3.2 and 13.4 times those of Pt/C, i.e. $0.88 \text{ A mg}_{\text{Pt}}^{-1}$ and 1.02 mA cm^{-2} , respectively.

In order to further reveal the intrinsic electrocatalytic activity, the TOF values for Pt-Ni ASs and Pt/C were calculated based on the estimated numbers of active sites (Figure S24).^[26] As summarized in Figure 4e, Pt-Ni ASs achieve the extremely high TOF value at the investigated potential region in 1.0 M KOH aqueous solution. Particularly, the TOF value of Pt-Ni ASs reaches $18.63 \text{ H}_2 \text{ s}^{-1}$ at the overpotential of 50 mV, which is much higher than that of Pt/C ($1.62 \text{ H}_2 \text{ s}^{-1}$) and other recently reported advanced HER electrocatalysts, such as Ru@C₂N ($1.66 \text{ H}_2 \text{ s}^{-1}$ at overpotential of 50 mV),^[26] Ni₅P₄ ($2.9 \text{ H}_2 \text{ s}^{-1}$ at overpotential of 200 mV),^[27] Ni-Mo nanopowders ($0.05 \text{ H}_2 \text{ s}^{-1}$ at overpotential of 100 mV),^[28] γ -Mo₂N ($0.07 \text{ H}_2 \text{ s}^{-1}$ at overpotential of 250 mV)^[29] and α -Mo₂C ($0.9 \text{ H}_2 \text{ s}^{-1}$ at overpotential of 200 mV)^[29] (Figure 4e). To the best of our knowledge, the Pt-Ni ASs possesses the greatest TOF value, proving that the Pt-Ni AS is a highly efficient electrocatalyst for HER. Additionally, the comparison of the overpotential at 10 mA cm^{-2} for Pt-Ni ASs with Pt/C and other recently reported HER electrocatalysts is also provided (Figure 4d, g and Table S4). A quite low overpotential of only 27.7 mV is required for Pt-Ni ASs to achieve the target current density (10 mA cm^{-2}), which is among the best in reported electrocatalysts. Moreover, the electrocatalytic stability of Pt-Ni ASs towards HER was investigated by a long-term cycling test. As shown in Figure 4f, almost no shift of the polarization curve was observed after 10,000 potential cycles from 0.1 V to -0.1 V (versus reversible hydrogen electrode (RHE)) in 1.0 M KOH aqueous solution. Importantly, as evidenced by the TEM characterization (Figure S25), there is no obvious change of shape, size and phase of Pt-Ni ASs after the electrocatalytic stability test. All the aforementioned results demonstrate the excellent catalytic activity and durability of Pt-Ni ASs for the HER under alkaline conditions.

The superior electrocatalytic performance of the Pt-Ni ASs could be attributed to the following reasons. First, the Pt-Ni ASs with highly anisotropic structure possess relatively large

surface area. Meanwhile, the small sharp-shaped Pt-rich nanoparticles on the end surfaces, i.e., {001} planes, and the few-layer Pt-rich shells on the side surfaces of the “arms” could provide abundant active sites and improve the atom utilization efficiency of Pt,^[30,31] which are favorable for the HER. Second, as demonstrated by the previous reports, the catalytic performance of noble metal-based nanostructure can be rationally modulated by their crystal phase,^[6,12,15,20] and those with *hcp* phase could show enhanced HER activity compared with their *fcc* phase, arising from the distinct atomic arrangement and electronic structure.^[6,32,33] In this work, the “arms” of Pt-Ni ASs possess an *hcp* phase, which is beneficial to the electrocatalytic HER activity. In addition, the change of coordination environment and chemical bonding at the crystal phase boundaries of the Pt-Ni ASs might also induce the change of electron band structure, thus leading to the enhancement in electrocatalytic activity.^[34-36] Third, the rough surfaces with rich atomic steps in the “arms” (Figure 1h) and the synergistic effect between Pt and Ni^[6,8,9] could also contribute to the HER activity of Pt-Ni ASs. Furthermore, the Ni oxide species arising from the surface oxidation (Figure 2f) may facilitate the water dissociation and thus improve the HER activity in alkaline environments.^[10]

In summary, for the first time, we have synthesized the well-crystalline lotus thalamus-shaped Pt-Ni ASs with Pt-rich surfaces and *hcp/fcc* crystal phases via a simple one-pot solvothermal method. The time-dependent experiments showed that the Ni-rich polyhedron-shaped nanoparticles were first formed, which then grew into branched nanostructures. Meanwhile, the galvanic replacement reaction between Ni branched nanostructures and Pt precursors in the solution and the subsequent facet-selective co-deposition of Pt and Ni atoms are responsible for the formation of the Pt-Ni ASs. Impressively, the as-synthesized Pt-Ni ASs exhibit superior electrocatalytic activity and stability towards HER under alkaline conditions compared to the commercial Pt/C and other reported electrocatalysts. Our work provides a new strategy for the synthesis of highly anisotropic superstructures with unique spatial heterogeneity, which could boost their promising applications in catalytic reactions.

Acknowledgement

Z.Z. and G. L. contributed equally to this work. This work was supported by MOE under AcRF Tier 2 (ARC 19/15, No. MOE2014-T2-2-093; MOE2015-T2-2-057; MOE2016-T2-2-103; MOE2017-T2-1-162) and AcRF Tier 1 (2016-T1-001-147; 2016-T1-002-051; 2017-T1-001-150), NTU under Start-Up Grant (M4081296.070.500000) in Singapore. L. G. acknowledges the National Natural Science Foundation of China (51522212). We would like to acknowledge the Facility for Analysis, Characterization, Testing and Simulation, Nanyang Technological University, Singapore, for use of their electron microscopy facilities. We also thank the XAFCA beamline of Singapore Synchrotron Light Source for supporting this project.

Received: ((will be filled in by the editorial staff))

Revised: ((will be filled in by the editorial staff))

Published online: ((will be filled in by the editorial staff))

- [1] H.-L. Liu, F. Nosheen, X. Wang, *Chem. Soc. Rev.* **2015**, *44*, 3056.
- [2] B. Lim, M. Jiang, P. H. Camargo, E. C. Cho, J. Tao, X. Lu, Y. Zhu, Y. Xia, *Science* **2009**, *324*, 1302.
- [3] C. Chen, Y. Kang, Z. Huo, Z. Zhu, W. Huang, H. L. Xin, J. D. Snyder, D. Li, J. A. Herron, M. Mavrikakis, M. Chi, K. L. More, Y. Li, N. M. Markovic, G. A. Somorjai, P. Yang, V. R. Stamenkovic. *Science* **2014**, *343*, 1339.
- [4] M. A. Boles, M. Engel, D. Talapin, *Chem. Rev.* **2016**, *116*, 11220.
- [5] R. He, Y.-C. Wang, X. Wang, Z. Wang, G. Liu, W. Zhou, L. Wen, Q. Li, X. Wang, X. Chen, J. Zeng, J. Hou, *Nat. Commun.* **2014**, *5*, 4327.
- [6] Z. Cao, Q. Chen, J. Zhang, H. Li, Y. Jiang, S. Shen, G. Fu, B.-A. Lu, Z. Xie, L. Zheng, *Nat. Commun.* **2017**, *8*, 15131.
- [7] H. Yin, S. Zhao, K. Zhao, A. Muqsit, H. Tang, L. Chang, H. Zhao, Y. Gao, Z. Tang, *Nat. Commun.* **2015**, *6*, 6430.
- [8] P. Wang, K. Jiang, G. Wang, J. Yao, X. Huang, *Angew. Chem. Int. Ed.* **2016**, *55*, 12859.
- [9] R. Subbaraman, D. Tripkovic, D. Strmcnik, K.-C. Chang, M. Uchimura, A. P. Paulikas, V. Stamenkovic, N. M. Markovic, *Science* **2011**, *334*, 1256.

- [10] R. Subbaraman, D. Tripkovic, K.-C. Chang, D. Strmcnik, A. P. Paulikas, P. Hirunsit, M. Chan, J. Greeley, V. Stamenkovic, N. M. Markovic, *Nat. Mater.* **2012**, *11*, 550.
- [11] P. Wang, X. Zhang, J. Zhang, S. Wan, S. Guo, G. Lu, J. Yao, X. Huang, *Nat. Commun.* **2017**, *8*, 14580.
- [12] Z. Fan, H. Zhang, *Chem. Soc. Rev.* **2016**, *45*, 63.
- [13] Z. Fan, X. Huang, Y. Chen, W. Huang, H. Zhang, *Nat. Protocols* **2017**, *12*, 2367.
- [14] X. Huang, S. Li, Z. Huang, S. Wu, X. Zhou, S. Li, C. L. Gan, F. Boey, C. A. Mirkin, H. Zhang, *Nat. Commun.* **2011**, *2*, 292.
- [15] K. Kusada, H. Kitagawa, *Adv. Mater.* **2016**, *28*, 1129.
- [16] J. Mao, W. Chen, D. He, J. Wan, J. Pei, J. Dong, Y. Wang, P. An, Z. Jin, W. Xing, H. Tang, Z. Zhuang, X. Liang, Y. Huang, G. Zhou, L. Wang, D. Wang, Y. Li, *Sci. Adv.* **2017**, *3*, e1603068.
- [17] N. Becknell, Y. Kang, C. Chen, J. Resasco, N. Kornienko, J. Guo, N. M. Markovic, G. A. Somorjai, V. R. Stamenkovic, P. Yang, *J. Am. Chem. Soc.* **2015**, *137*, 15817.
- [18] B.-J. Hwang, L. S. Sarma, J. -M. Chen, C. -H. Chen, S. -C. Shih, G. -R. Wang, D. -G. Liu, J. -F. Lee, M. -T. Tang, *J. Am. Chem. Soc.* **2005**, *127*, 11140.
- [19] H. Duan, N. Yan, R. Yu, C. -R. Chang, G. Zhou, H. -S. Hu, H. Rong, Z. Niu, J. Mao, H. Asakura, T. Tanaka, P. J. Dyson, J. Li, Y. Li, *Nat. Commun.* **2014**, *5*, 3093.
- [20] A.-X. Yin, W.-C. Liu, J. Ke, W. Zhu, J. Gu, Y.-W. Zhang, C.-H. Yan, *J. Am. Chem. Soc.* **2012**, *134*, 20497.
- [21] F. Saleem, Z. Zhang, B. Xu, X. Xu, P. He, X. Wang, *J. Am. Chem. Soc.* **2013**, *135*, 18304.
- [22] X. Xia, Y. Wang, A. Ruditskiy, Y. Xia, *Adv. Mater.* **2013**, *25*, 6313.
- [23] P. Yang, X. Yuan, H. Hu, Y. Liu, H. Zheng, D. Yang, L. Chen, M. Cao, Y. Xu, Y. Min, Y. Li, Q. Zhang, *Adv. Funct. Mater.* **2017**, *28*, 1704774.

- [24] A. P. LaGrow, S. Cheong, J. Watt, B. Ingham, M. F. Toney, D. A. Jefferson, R. D. Tilley, *Adv. Mater.* **2013**, 25, 1552.
- [25] J.-X. Liu, H.-Y. Su, D.-P. Sun, B.-Y. Zhang, W.-X. Li, *J. Am. Chem. Soc.* **2013**, 135, 16284.
- [26] J. Mahmood, F. Li, S.-M. Jung, M. S. Okyay, I. Ahmad, S.-J. Kim, N. Park, H. Y. Jeong, J.-B. Baek, *Nat. Nanotechnol.* **2017**, 12, 441.
- [27] A. B. Laursen, K. R. Patraju, M. J. Whitaker, M. Retuerto, T. Sarkar, N. Yao, K. V. Ramanujachary, M. Greenblatt, G. C. Dismukes, *Energy Environ. Sci.* **2015**, 8, 1027.
- [28] J. R. McKone, B. F. Sadtler, C. A. Werlang, N. S. Lewis, H. B. Gray, *ACS Catal.* **2013**, 3, 166.
- [29] L. Ma, L. R. L. Ting, V. Molinari, C. Giordano, B. S. Yeo, *J. Mater. Chem. A* **2015**, 3, 8361.
- [30] L. Gan, C. Cui, M. Heggen, F. Dionigi, S. Rudi, P. Strasser, *Science* **2014**, 346, 1502.
- [31] Z. Zhang, Z. Luo, B. Chen, C. Wei, J. Zhao, J. Chen, X. Zhang, Z. Lai, Z. Fan, C. Tan, M. Zhao, Q. Lu, B. Li, Y. Zong, C. Yan, G. Wang, Z. Xu, H. Zhang, *Adv. Mater.* **2016**, 28, 8712.
- [32] Z. Fan, Z. Luo, X. Huang, B. Li, Y. Chen, J. Wang, H. Zhang, *J. Am. Chem. Soc.* **2016**, 138, 1414.
- [33] Z. Fan, H. Zhang, *Acc. Chem. Res.* **2016**, 49, 2841.
- [34] D. O. Scanlon, C. W. Dunnill, J. Buckeridge, S. A. Shevlin, A. J. Logsdail, S. M. Woodley, C. R. A. Catlow, M. J. Powell, R. G. Palgrave, I. P. Parkin, G. W. Watson, T. W. Keal, P. Sherwood, A. Walsh, A. A. Sokol, *Nat. Mater.* **2013**, 12, 798.
- [35] Y. Chen, Z. Fan, Z. Luo, X. Liu, Z. Lai, B. Li, Y. Zong, L. Gu, H. Zhang, *Adv. Mater.* **2017**, 29, 1701331.
- [36] Z. Zhang, B. Xu, X. Wang, *Chem. Soc. Rev.* **2014**, 43, 7870.

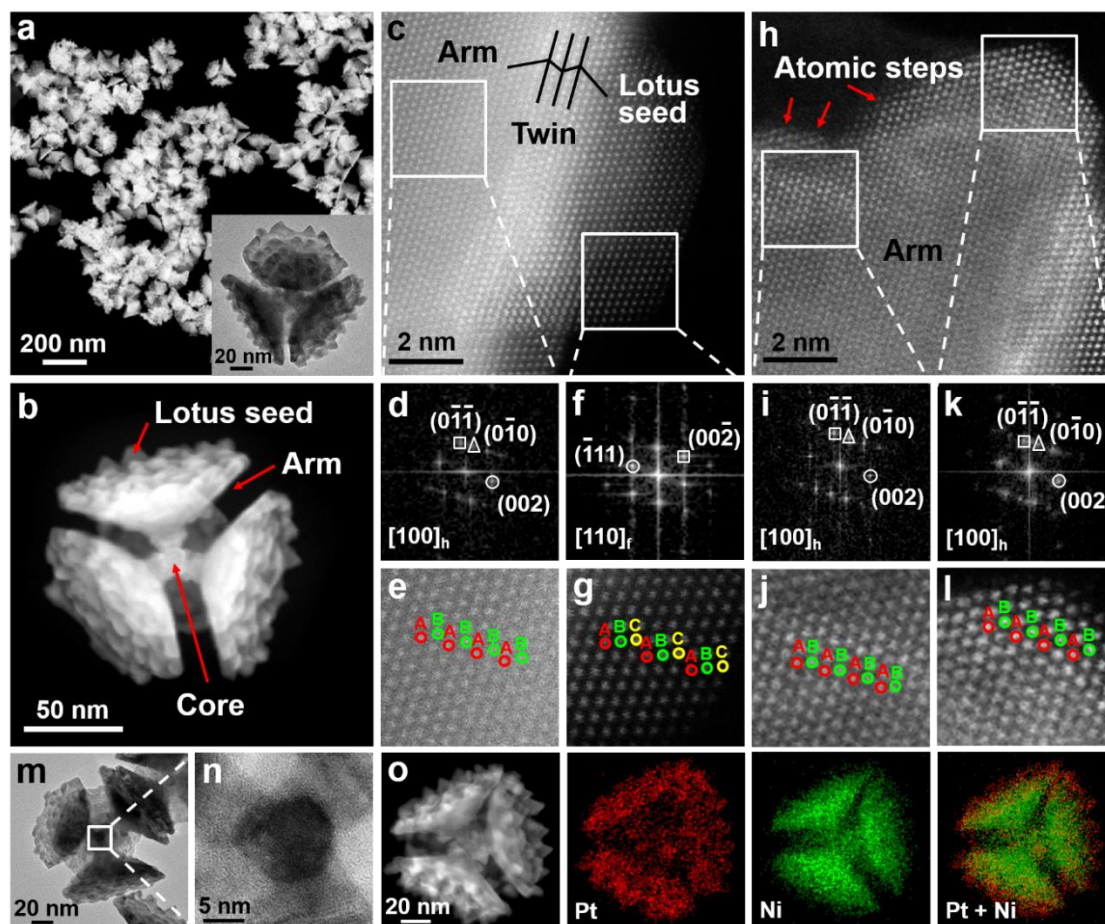


Figure 1. a,b) HAADF-STEM images of the Pt-Ni ASs. Inset in (a): TEM image of a single Pt-Ni AS. c) Aberration-corrected HAADF-STEM image of the “lotus seed” grown on the end surface of an “arm” of the Pt-Ni AS. d,f) FFT patterns and e,g) magnified aberration-corrected HAADF-STEM images taken from the corresponding two white squares in (c). h) Aberration-corrected HAADF-STEM image of a side surface of an “arm” of the Pt-Ni AS. i,k) FFT patterns and j,l) magnified aberration-corrected HAADF-STEM images taken from the corresponding two white squares in (h). m) TEM and n) magnified TEM images taken from the white square in (m) of a Pt-Ni AS. o) HAADF-STEM and the corresponding EDS elemental mapping images of a typical Pt-Ni AS.

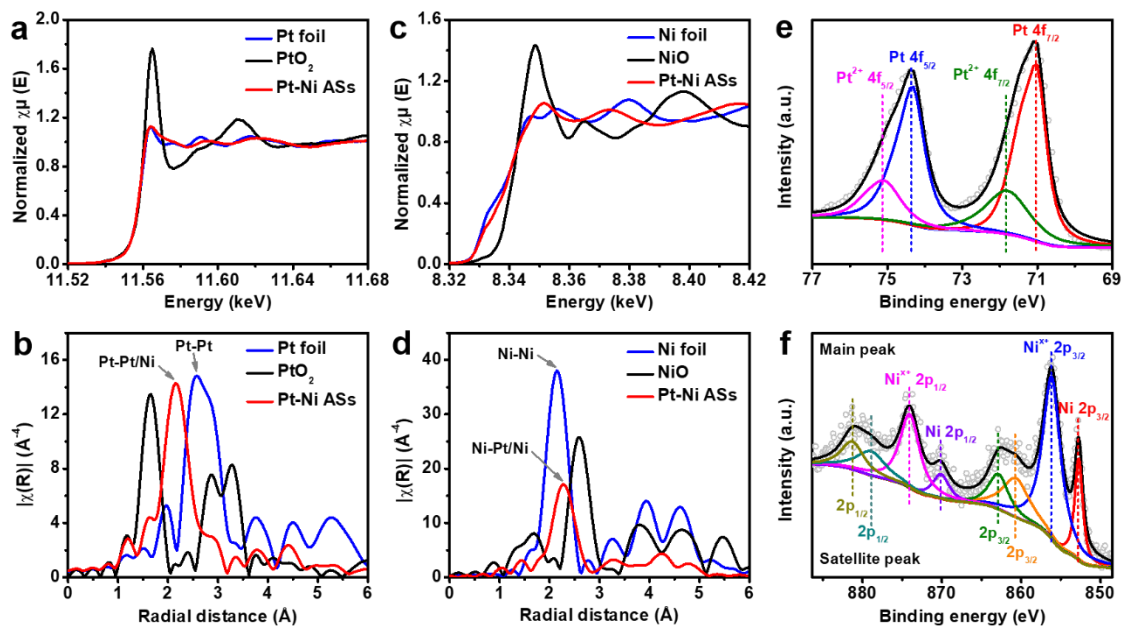


Figure 2. a) The XANES and b) the Fourier transforms of EXAFS spectra of Pt-Ni ASs, Pt foil and PtO₂ for the Pt L₃-edge. c) The XANES and d) the Fourier transforms of EXAFS spectra of Pt-Ni ASs, Ni foil and NiO for the Ni K-edge. e) Pt 4f and f) Ni 2p XPS spectra of Pt-Ni ASs.

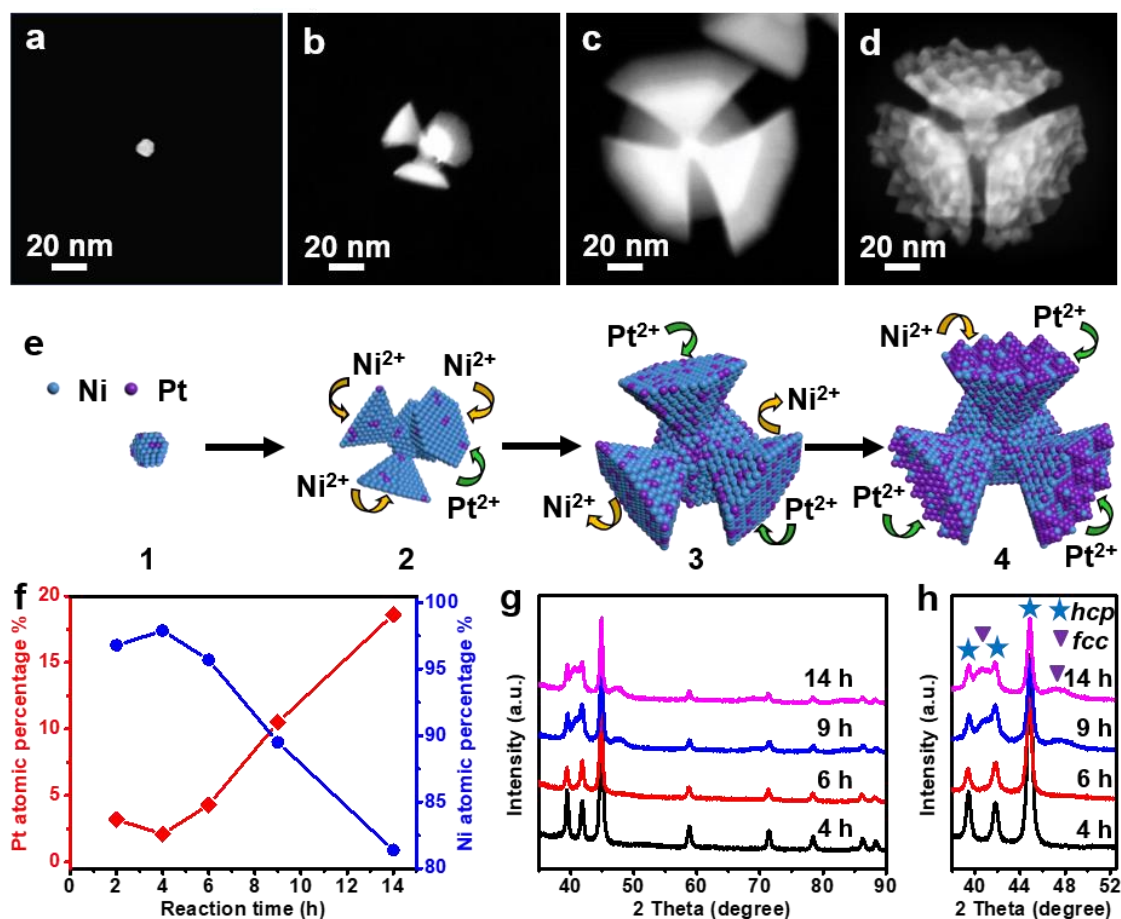


Figure 3. HAADF-STEM images of the products obtained at different reaction time: a) 2 h, b) 4 h, c) 6 h, and d) 9 h. e) Schematic illustration of the corresponding products shown in (a–d) obtained at different reaction time. f) Pt and Ni atomic percentage of the products obtained at different reaction time. g) XRD patterns and h) the corresponding magnified XRD patterns of the products obtained at different reaction time.

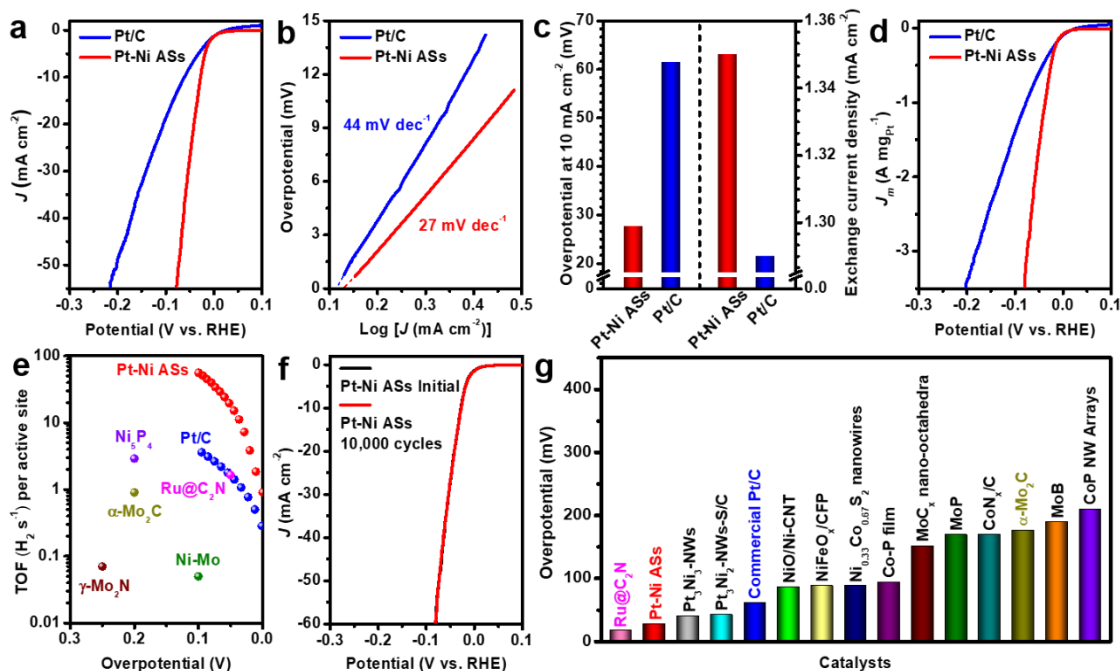


Figure 4. a) Polarization curves of Pt-Ni ASs and commercial Pt/C. Linear sweep voltammetry was conducted in 1.0 M KOH aqueous solution at a scan rate of 5.0 mV s⁻¹. b) Tafel plots obtained from the polarization curves in (a). c) Overpotentials at current density of 10.0 mA cm⁻² (left) and exchange current densities (right) of Pt-Ni ASs and commercial Pt/C. d) Mass activities of Pt-Ni ASs and commercial Pt/C. e) Comparison of the TOF values of Pt-Ni ASs, commercial Pt/C and previously reported electrocatalysts. The TOF values of Pt-Ni ASs and commercial Pt/C were calculated based on the number of active sites using the Equation S2 in Supporting Information. Note that the TOF values of Ru@C₂N,^[26] Ni₅P₄,^[27] Ni-Mo,^[28] and both α-Mo₂C and γ-Mo₂N^[29] were calculated based on number of active Ru atoms, total Ni atoms, surface Ni and Mo atoms, and surface Mo atoms in the corresponding catalysts, respectively. f) Durability test of Pt-Ni ASs. The polarization curves were recorded before and after 10,000 potential cycles in 1.0 M KOH aqueous solution from 0.1 to -0.1 V (vs. RHE). g) Comparison of the overpotentials of Pt-Ni ASs, commercial Pt/C and previously reported electrocatalysts at current density of 10 mA cm⁻² in 1.0 M KOH aqueous solution.

The well-crystalline lotus thalamus-shaped Pt-Ni anisotropic superstructures (ASSs) with unique *hcp/fcc* crystal phases and Pt-rich surface are synthesized via a simple one-pot solvothermal method. The obtained Pt-Ni ASSs exhibit superior electrocatalytic activity and stability towards hydrogen evolution reaction under alkaline conditions compared to the commercial Pt/C and other reported electrocatalysts.

Keywords: Alloy, anisotropic structure, crystal structure, electrocatalysis, hydrogen evolution reaction.

By Zhicheng Zhang,¹ Guigao Liu,¹ Xiaoya Cui,¹ Bo Chen,¹ Yihan Zhu,² Yue Gong,³ Faisal Saleem,¹ Shibo Xi,⁴ Yonghua Du,⁴ Armando Borgna,⁴ Zhuangchai Lai,¹ Qinghua Zhang,³ Bing Li,⁵ Yun Zong,⁵ Yu Han,⁶ Lin Gu,³ and Hua Zhang^{1,*}

Crystal Phase and Architecture Engineering of Lotus Thalamus-Shaped Pt-Ni Anisotropic Superstructures for Highly Efficient Electrochemical Hydrogen Evolution

TOC

